SUPPLEMENTARY INFORMATION

Ribosomal initiation complex-driven changes in the stability and dynamics of initiation factor 2 regulate the fidelity of translation initiation

Jiangning Wang, Kelvin Caban, and Ruben L. Gonzalez, Jr.

Department of Chemistry, Columbia University, New York, NY 10027.

To whom correspondence should be addressed: Ruben L. Gonzalez Jr., Department of Chemistry, Columbia University, 3000 Broadway, MC3126, New York, NY 10027, USA, Tel.: (212) 854-1096; Fax: (212) 932-1289; Email: rlg2118@columbia.edu

TABLE OF CONTENTS

SUPPLEMENTARY FIGURES

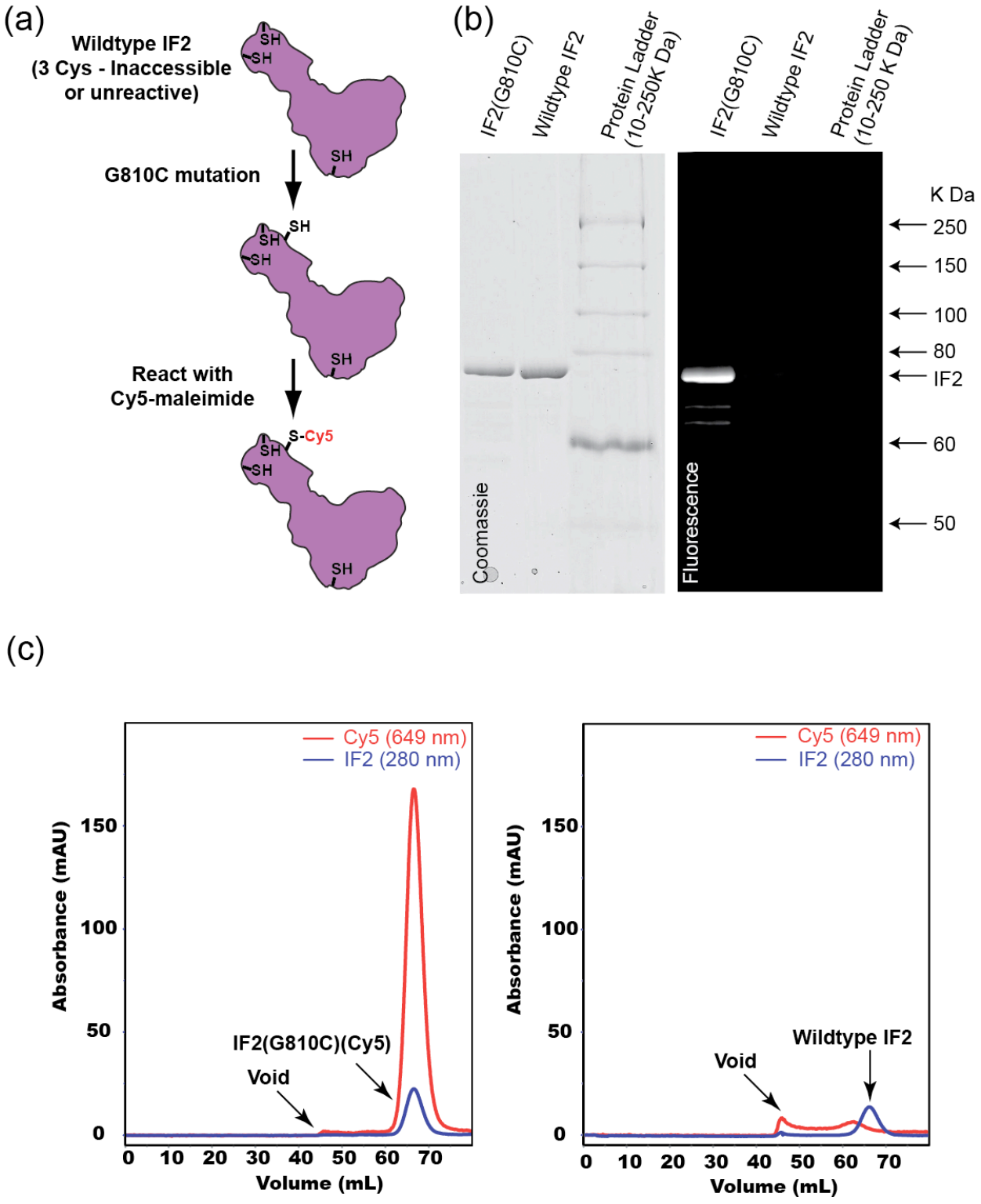

Supplementary Figure 1. Generation and Cy5 FRET-acceptor labeling of an initiation factor (IF) 2 variant containing a glycine-to-cysteine mutation at amino acid position 810 (IF2(G810C); note

that the IF2 amino acid numbering used throughout this work corresponds to the α isoform of IF2). **(a)** Cartoon schematic outlining the protocol for mutagenizing wildtype IF2 to generate IF2(G810C) and for labeling of IF2(G810C) with maleimide-derivatized Cy5. Wildtype *Escherichia coli* IF2 contains three naturally occurring, but presumably buried and/or inaccessible, cysteines. Starting with this wildtype IF2, a fourth cysteine was introduced by site-directed mutagenesis of a phylogenetically variable, and presumably solvent accessible, glycine at position 810. The four-cysteine-containing IF2(G810C) was then reacted with maleimide-derivatized Cy5 under conditions in which only the presumably solvent-accessible G810C cysteine was significantly reactive towards the maleimide-derivatized Cy5 (Materials and Methods). **(b)** Sodium dodecyl sulfate polyacrylamide gel electrophoresis (SDS-PAGE) analysis of IF2(G810C) and wildtype IF2 that have been reacted with maleimide-derivatized Cy5. Coomassie staining and fluorescence scanning of the SDS-PAGE gel demonstrates very high-efficiency labeling of IF2(G810C) with Cy5 and very low-efficiency labeling of wildtype IF2 with Cy5. **(c)** Size-exclusion chromatographic analysis of IF2(G810C) and wildtype IF2 which have been reacted with maleimide-derivatized Cy5. IF2(G810C) (left panel) and wildtype IF2 (right panel) were reacted with maleimide-derivatized Cy5 and loaded onto a Superdex 200 size-exclusion chromatography column. In both cases a small fraction of IF2 is aggregated and elutes at a retention volume of ~45 mL, a retention volume that is consistent with the void volume of the column. The remainder of IF2 elutes in a single, well-defined peak at a retention volume of ~66 mL, consistent with the expected retention volume for a protein with the molecular weight of IF2 (78.8 kDa). Integration of the areas under the peaks observed at ~66 mL using the 280 nm signal (corresponding to the absorbance of the IF2 protein) and the 649 nm signal (corresponding to the absorbance of Cy5) for both IF2(G810C) and wildtype IF2 demonstrates an ~95% Cy5 labeling efficiency for IF2(G810C) and an ~2% Cy5 labeling efficiency for wildtype IF2.

(a)

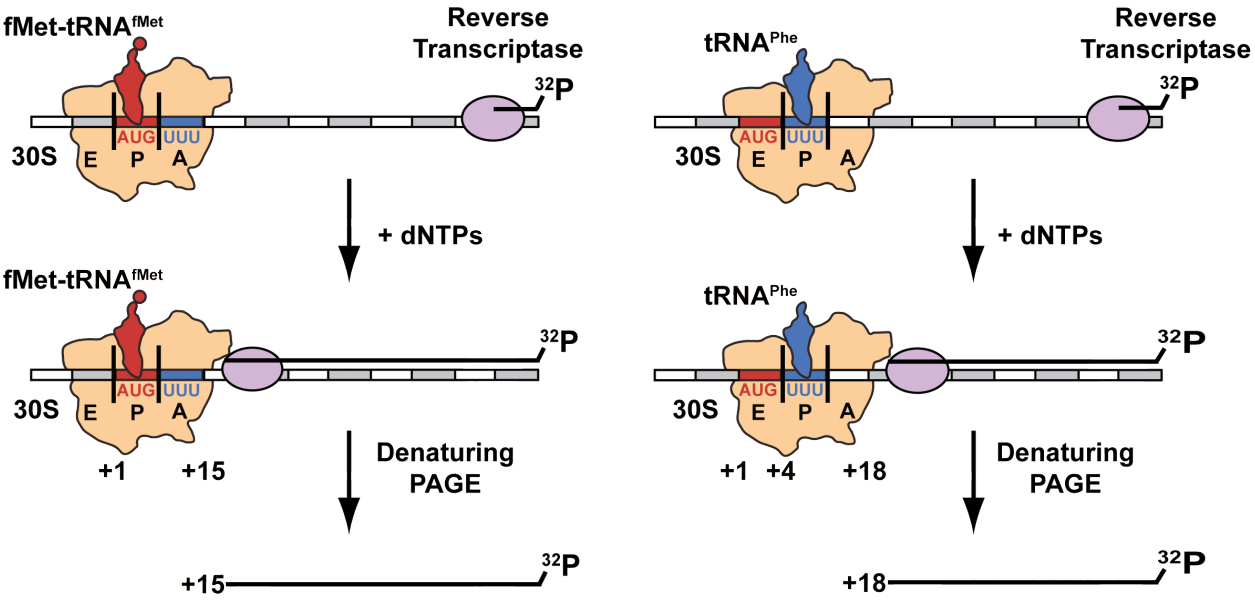

(b)

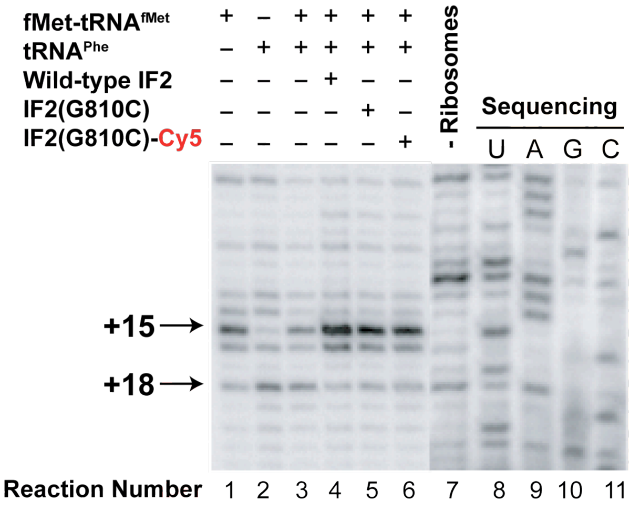

Supplementary Figure 2. Standard, primer extension inhibition, or "toeprinting", -based IF2 activity assay. **(a)** Cartoon schematic outlining the previously published[1-3] toeprinting-based assay that was used to test the ability of wildtype IF2, IF2(G810C), and IF2(Cy5) to select initiator transfer RNA (N-formylmethionyl-transfer RNA; fMet-tRNA^{fMet}) over elongator tRNAs within the 30S initiation complex (30S IC). 30S ICs were assembled using the mRNA$_{pri-ext}$ messenger RNA (mRNA) to which a 5'-[^{32}P]-labeled DNA primer had been pre-annealed to a primer binding site that was 43 nucleotides 3' to the A nucleotide of the AUG start codon (Supplementary Note 1). Subsequent reverse transcription of the primer-annealed mRNA$_{pri-ext}$ is blocked when the reverse transcriptase encounters an mRNA-bound 30S subunit, thereby

generating a 5'-[^{32}P]-labeled complementary DNA (cDNA) of a defined length, called a ''toeprint.'' In $mRNA_{pri-ext}$, the AUG start codon encoding fMet-$tRNA^{fMet}$ is followed by a UUU triplet at the second codon position, which encodes Phe-$tRNA^{Phe}$. Binding of fMet-$tRNA^{fMet}$ to the AUG start codon at the P site of the 30S subunit generates a toeprint at a position that is 15 nucleotides 3' to the A nucleotide of the AUG start codon (*i.e.*, a +15 toeprint), whereas binding of $tRNA^{Phe}$ to the UUU codon at the P site of the 30S subunit generates a toeprint at a position that is 18 nucleotides 3' to the A nucleotide of the AUG start codon (*i.e.*, a +18 toeprint). Selection of fMet-$tRNA^{fMet}$ over $tRNA^{Phe}$ using the $mRNA_{pri-ext}$ can be assessed by comparing the intensity of the +15 toeprint relative to the intensity of the +18 toeprint on a 9% sequencing polyacrylamide electrophoresis gel. **(b)** Representative sequencing gel analysis of a series of toeprinting reactions. Six reactions were performed. Reactions 1 and 2 were performed in the absence of IF2, but in the presence of either fMet-$tRNA^{fMet}$ (Reaction 1) or $tRNA^{Phe}$ (Reaction 2), which demonstrated that both fMet-$tRNA^{fMet}$ and $tRNA^{Phe}$ can efficiently bind to the P site of the 30S subunit and generate strong +15 and +18 toeprints, respectively. Reactions 3–6 were run in the presence of equimolar amounts of fMet-$tRNA^{fMet}$ and $tRNA^{Phe}$ and in either the absence of IF2 (Reaction 3) or the presence of wildtype IF2 (Reaction 4), IF2(G810C) (Reaction 5), or IF2(Cy5) (Reaction 6). In the absence of IF2, the +15 and +18 toeprints exhibited approximately equal intensity, consistent with the inability of the mRNA-bound 30S subunit to discriminate between fMet-$tRNA^{fMet}$ and $tRNA^{Phe}$ in the absence of IF2. In the presence of wildtype IF2, IF2(G810C), or IF2(Cy5), however, a strong +15 toeprint and a missing or weak +18 toeprint were observed, demonstrating the ability of wildtype IF2, IF2(G810C), and IF2(Cy5) to select fMet-$tRNA^{fMet}$ over $tRNA^{Phe}$. In addition to the reactions described above, five control reactions were also performed. Reaction 7, which was a toeprinting reaction performed in the absence of the 30S subunit, tRNAs, and IF2, was used to identify intrinsic sites on $mRNA_{pri-ext}$ where reverse transcriptase encounters relatively strong stops in response to local secondary structures within the mRNA itself. Reactions 8–11 were primer-extension sequencing reactions used to confirm the locations of the +15 and +18 toeprints. Collectively, the results of these toeprinting assays demonstrated that IF2(G810C) and IF2(Cy5) are able to discriminate fMet-$tRNA^{fMet}$ from elongator tRNAs in a manner that is indistinguishable from wildtype IF2.

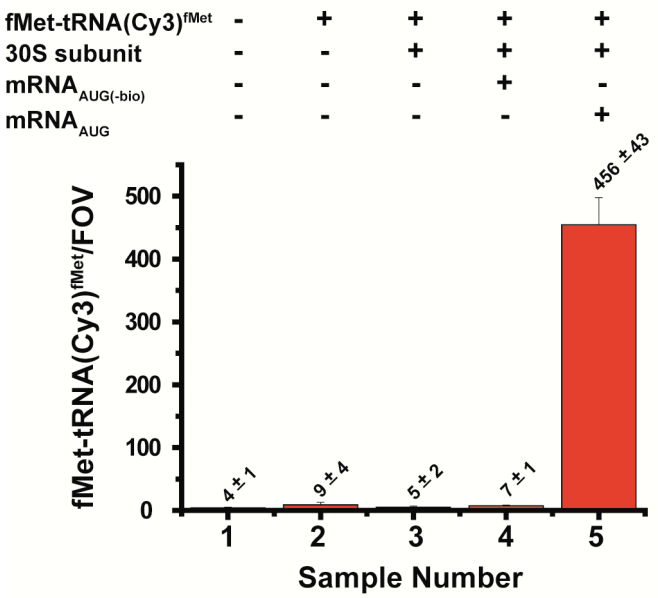

Supplementary Figure 3. The specificity with which 30S ICs assembled on 5'-biotinylated mRNAs are tethered to the polyethylene glycol (PEG)/biotinylated-PEG-derivatized surface of the quartz microfluidic flowcells used for total internal reflection fluorescence (TIRF) microscopy using a biotin-streptavidin-biotin bridge. To confirm that the single, surface-localized fMet-tRNA(Cy3)^{fMet}s observed using TIRF microscopy were indeed reporting on intact 30S ICs that were tethered to the flowcell surface *via* their 5'-biotinylated mRNAs, we prepared a series of control 30S $IC_{-1/3}$ samples in which the 30S subunit, the mRNA, or the biotin moiety at the 5' end of the mRNA were systematically excluded from the assembly reaction. The resulting 30S $IC_{-1/3}$-based control samples were diluted to 0.5 nM, loaded into flowcells, incubated, washed, and imaged as described in the Materials and Methods, with the exception that IF2(Cy5) was not added to the samples. Each 30S $IC_{-1/3}$-based control sample was analyzed by imaging 14 fields-of-view (FOVs) in which the observation period per FOV was 500 ms (*i.e.*, five 100 ms frames per FOV). To minimize slight differences arising from day-to-day variations in imaging parameters and batch-to-batch variations in flowcell performance, all five 30S $IC_{-1/3}$-based control samples comprising a single tethering specificity test were always performed on the same day, using the same imaging parameters and the same batch of flowcells. Each five-frame movie was processed by generating a single composite image in which each pixel contains the maximum intensity value that that pixel recorded in any of the five frames of the movie. Single fMet-tRNA(Cy3)^{fMet}s were then discriminated from the background noise and identified by applying an intensity threshold to the composite image. The intensity threshold was determined by visual inspection and the identical threshold was applied to each of the composite images arising from all 14 FOVs recorded for all five 30S $IC_{-1/3}$-based control samples comprising the specificity test. For each 30S $IC_{-1/3}$-based control sample, the two FOVs containing the largest number of single fMet-tRNA(Cy3)^{fMet}s and the two FOVs containing the smallest number of single fMet-tRNA(Cy3)^{fMet}s were discarded and the remaining 10 FOVs were used to calculate the average number of single fMet-tRNA(Cy3)^{fMet}s observed per FOV (fMet-tRNA(Cy3)^{fMet}/FOV). The calculation results are indicated above each bar in the bar graph in the form of average number ± standard deviation. The results of these experiments demonstrated that ≥ 98% of the single, surface-localized fMet-tRNA(Cy3)^{fMet}s observed using TIRF microscopy are localized to the surface *via* their interactions with 30S subunits that are themselves tethered to the flowcell surface *via* their interactions with a 5'-biotinylated mRNA.

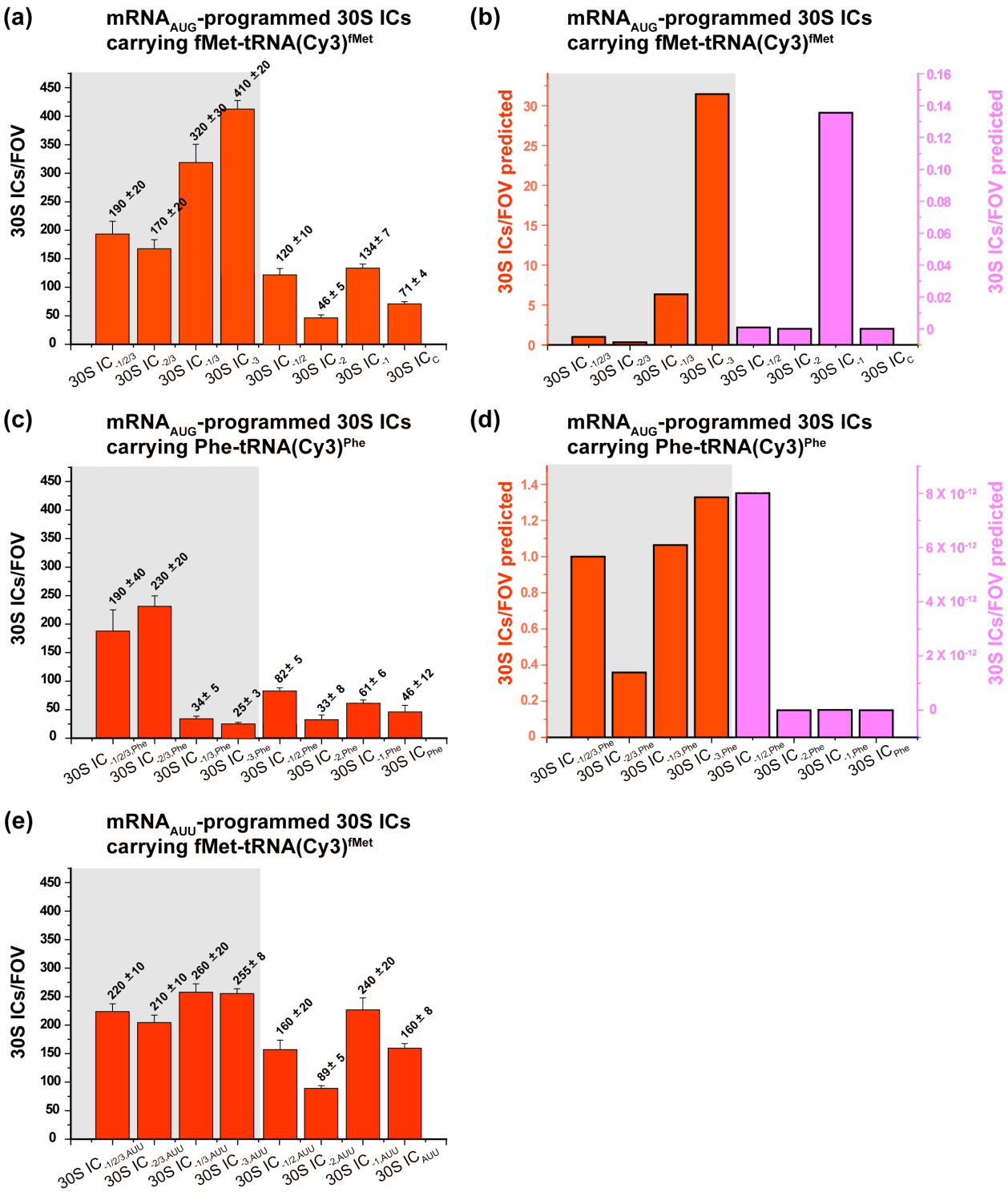

Supplementary Figure 4. The stability of aa-tRNA binding to the P site of the 30S IC. The stability of aa-tRNA binding to the P site of the 30S IC during translation initiation is strongly dependent on the presence *versus* the absence of the three IFs as well as on the identities of the aa-tRNA[2,4] and the codon[5] positioned within the P site. To systematically characterize the stability of aa-tRNA binding to the P site of the 30S IC in our *in vitro* translation system, we prepared a set of canonical, pseudo, and non-canonical 30S IC control samples. In each set of

control samples, an identical series of eight 30S ICs were prepared encompassing all eight possible combinations of the three unlabeled IFs. The eight 30S ICs were prepared as described in the Materials and Methods, with the exception that, when present in the 30S IC, 0.9 μM unlabeled wildtype IF2 was included in the assembly reaction as well as in all subsequent dilution and wash steps to ensure that the 30S IC was saturated with unlabeled IF2. **(a)** The stability of fMet-tRNA(Cy3)^{fMet} binding to mRNA$_{AUG}$-programmed, canonical 30S ICs. The 30S IC samples were diluted to 0.3 nM, loaded into flowcells, incubated, washed and imaged as described in the Materials and Methods. The *x* axis lists the various 30S ICs containing different combinations of IFs that were tested. 14 FOVs were imaged per sample using a short observation period of 500 ms per FOV (*i.e.*, five 100 ms frames per FOV) to minimize photobleaching of the Cy3 fluorophore. The resulting five-frame movie of each FOV was processed and single fMet-tRNA(Cy3)^{fMet}-containing 30S ICs were discriminated from the background noise as described in Supplementary Fig. 3. For each sample, the two FOVs containing the largest number of single 30S ICs and the two FOVs containing the smallest number of single 30S ICs were discarded and the remaining 10 FOVs were used to calculate the average number and standard deviation of the number of single 30S ICs observed per FOV (30S ICs/FOV). The calculation results are indicated above each bar in the bar graph in the form of average number ± standard deviation. Samples in which the 30S IC was assembled in the absence of IF3 are shaded in grey. **(b)** Predicted relative number of fMet-tRNA(Cy3)^{fMet}-containing 30S ICs/FOV for the 30S ICs depicted in (a). The predicted relative number of fMet-tRNA(Cy3)^{fMet}-containing 30S ICs/FOV was calculated using the value of the equilibrium dissociation constant for the interaction of fMet-tRNA^{fMet} with the 30S IC ($K_{d,tRNA}$) and the rate with which fMet-tRNA^{fMet} dissociates from the 30S IC ($k_{d,tRNA}$) as determined by Antoun, *et al*.[4] using ensemble kinetic measurements of 30S ICs analogous to the 30S ICs in (a) under experimental conditions similar to those reported here. For each sample, we have assumed that the 30S ICs/FOV that was ultimately observed in the experiment was a convolution of: (i) the equilibrium concentration of fMet-tRNA(Cy3)^{fMet}-bound 30S IC that was established during surface tethering of the 30S IC (characterized by $K_{d,tRNA}$) and (ii) $k_{d,tRNA}$ during the washing and imaging steps, which, as described in the Materials and Methods, was standardized to 5 min (represented by t) for each sample. Thus, the expected 30S ICs/FOV for each sample was proportional to $(1/K_{d,tRNA})[\exp(-k_{d,tRNA}\ t)]$. The 30S ICs/FOVs for all the samples were normalized to the expected 30S IC/FOV of 30S IC$_{-1/2/3}$ to obtain relative 30S ICs/FOV predicted. Samples assembled in the absence of IF3 (shaded in grey) are plotted using red bars and were scaled using the left-hand-side *y* axis that is shown in red, while samples assembled in the presence of IF3 are plotted using pink bars and were scaled using the right-hand-side y axis shown in pink. **(c)** The stability of Phe-tRNA(Cy3)^{Phe} binding to the mRNA$_{AUG}$-programmed, pseudo 30S ICs. The experiments were performed exactly as described in (a) with the exception that Phe-tRNA(Cy3)^{Phe} was used in place of fMet-tRNA(Cy3)^{fMet}. The data analysis was carried out and the bar graphs were plotted exactly as described in (a). **(d)** Predicted relative number of 30S ICs/FOV for the 30S ICs depicted in (c). The calculations were performed and the bar graphs were plotted exactly as described in (b), with the exception that values of $K_{d,tRNA}$ and $k_{d,tRNA}$ corresponding to Phe-tRNA^{Phe}, rather than fMet-tRNA^{fMet}, were used in the calculations. **(e)** The stability of fMet-tRNA(Cy3)^{fMet} binding to the mRNA$_{AUU}$-programmed, non-canonical 30S ICs. The experiments were performed exactly as described in (a) with the exception that mRNA$_{AUU}$ was used in place of mRNA$_{AUG}$ and the 30S IC samples were diluted to 0.5 nM instead of 0.3 nM prior to loading into the flowcells. The data analysis was carried out and the bar graphs were plotted exactly as described in (a). Collectively, the results of these control experiments provide further evidence that the IFs used in the present work have biochemical activities that are consistent with previous studies.

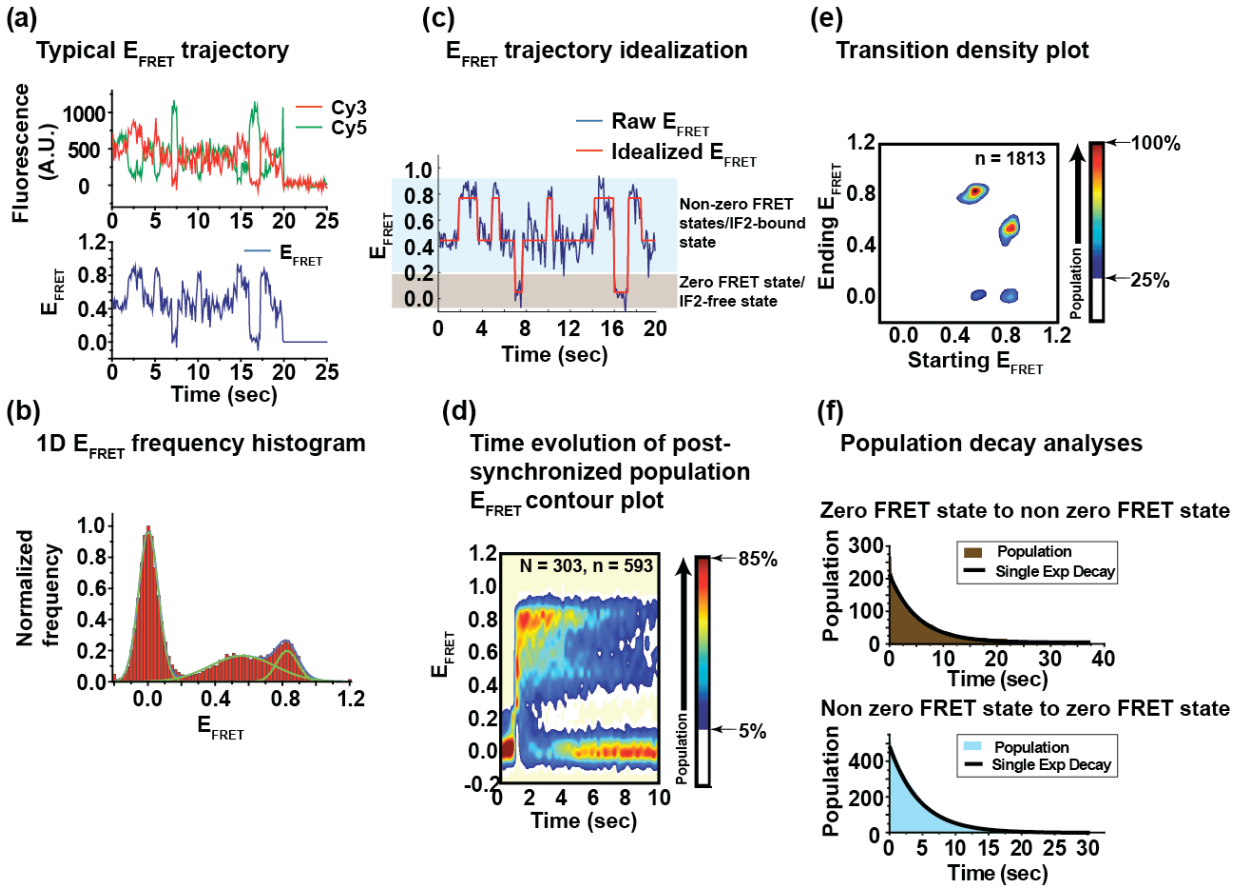

Supplementary Figure 5. smFRET data analysis. **(a)** Cy3 and Cy5 emission intensity *versus* time and E_{FRET} *versus* time trajectories. Representative bleedthrough- and baseline-corrected Cy3 and Cy5 emission intensities *versus* time trajectories are shown in green and red, respectively. The corresponding E_{FRET} *versus* time trajectory, calculated using $E_{FRET} = I_{Cy5}/(I_{Cy3} + I_{Cy5})$, where I_{Cy3} and I_{Cy5} are the bleedthrough- and baseline-corrected Cy3 and Cy5 emission intensities, respectively, is shown in blue. **(b)** One-dimensional E_{FRET} histogram. The range of –0.2 to 1.2 E_{FRET} was separated into 70 bins. The histogram was generated by plotting the aggregate number of time points across the entire set of E_{FRET} trajectories that occupy the range of E_{FRET} values specified by each bin. The histogram was normalized to the most populated bin. The resulting E_{FRET} histogram was fitted with multiple Gaussian distributions using Origin 7.0 in order to obtain a preliminary estimate of the number of FRET states present in the set of trajectories (Supplementary Note 2). The contours of the three fitted Gaussian distributions are shown in green and the sum of the three fitted Gaussian distributions is shown in blue. **(c)** Idealization of raw E_{FRET} trajectories. Idealization of raw E_{FRET} trajectories was accomplished using the hidden Markov model algorithms implemented within the HaMMy (http://bio.physics.illinois.edu/HaMMy.asp)[6] and, when specified, the vbFRET (http://vbfret.sourceforge.net)[7] software suites. The resulting idealized E_{FRET} trajectories were used to determine the number of FRET states present in the set of E_{FRET} trajectories and the centers of each of these FRET states (Supplementary Note 2). The non-zero FRET states that collectively encompass the aggregate non-zero FRET state that corresponds to the IF2-bound state of the 30S IC are shaded in cyan and the zero FRET state that corresponds to the IF2-free state of the 30S IC is shaded in brown. **(d)** Surface contour plot of the time evolution of population FRET

arising from post-synchronization of IF2 binding events. The plot was generated by superimposing the raw E_{FRET} corresponding to each IF2 binding event across the entire set of E_{FRET} trajectories such that the first time point of the raw E_{FRET} corresponding to each IF2 binding event was post-synchronized to the 1 sec time point of the surface contour plot. For the purposes of generating these plots, an IF2 binding event was defined as an event in which the idealized E_{FRET} crossed from $E_{FRET} < 0.2$ to $E_{FRET} \geq 0.2$, remained at $E_{FRET} \geq 0.2$ for one or more time points, and subsequently re-crossed from $E_{FRET} \geq 0.2$ to $E_{FRET} < 0.2$. The range of –0.2 to 1.2 E_{FRET} was separated into 24 bins. The range of 0 to 10 sec was separated into 50 bins. The resulting two-dimensional histogram was normalized to the most populated bin in the plot. The lower-and upper-bound thresholds determining whether data appears in the surface contour plot were 5% and 85% of the most populated bin, respectively. The z axis of the surface contour was plotted from tan (lowest population plotted) to red (highest population plotted) as indicated in the population color bar. "N" indicates the total number of E_{FRET} *versus* time trajectories and "n" indicates the total number of individual IF2 binding events used to generate the surface contour plot. **(e)** Transition density plot. The transition density plot (TDP) was generated by plotting the "Starting E_{FRET}" *versus* the "Ending E_{FRET}" for each transition as a surface contour plot of a two-dimensional E_{FRET} histogram. To minimize the potential impact of artifacts in the TDPs arising from overfitting of the raw E_{FRET} trajectories by the HMM algorithm used to generate the idealized E_{FRET} trajectories[8,9] (Supplementary Note 2) and/or by the time-domain binning of the continuous-time E_{FRET} *versus* time signal that is recorded by the electron-multiplying charge-coupled device (EMCCD) camera detector on the TIRF microscope[8], two post-processing steps were applied to the idealized E_{FRET} trajectories prior to plotting the TDPs: (i) because transitions between FRET states separated by $E_{FRET} < 0.1$ cannot generally be distinguished from noise, transitions in the idealized E_{FRET} trajectories that were composed of a change in $E_{FRET} < 0.1$ (~1% of the total number of transitions in the idealized E_{FRET} trajectories) were ignored and (ii) excursions to any FRET state lasting only a single time point (20% of the total number of excursions to any FRET state) were clustered with the FRET state exhibiting the closest E_{FRET} to the single time point. TDPs were then plotted using these post-processed, idealized E_{FRET} trajectories. The range of –0.2 to 1.2 E_{FRET} was separated into 24 bins. The resulting histogram was normalized to the most populated bin in the plot and the lower-and upper-bound thresholds determining whether data appears in the transition density plot were 25% and 100% of the most populated bin, respectively. The z axis of the surface contour was plotted from tan (lowest population plotted) to red (highest population plotted) as indicated in the population color bar. "n" indicates the total number of transitions used to generate the transition density plot. **(f)** Curve fitting-based population decay analyses of the zero FRET state and the aggregate non-zero FRET state. The number of 30S ICs in the zero FRET state prior to transitioning to any non-zero FRET state as a function of time is plotted in the upper panel as a population decay histogram and is fitted with a single-exponential decay function of the form $y = y_{0,zero} + A_{zero}[\exp(-x/\tau_{zero})]$, where A_{zero} is the amplitude, τ_{zero} is the lifetime of the zero FRET state, and $y_{0,zero}$ is the offset. The apparent rate of IF2 association, $k_{a,app}$, is given by $1/((\tau_{zero})([IF2]))$. Likewise, the number of 30S ICs in the aggregate non-zero FRET state prior to transitioning to the zero FRET state as a function of time is plotted in the lower panel as a population decay histogram and is fitted with a single-exponential decay function of the form $y = y_{0,non-zero} + A_{non-zero}[\exp(-x/\tau_{non-zero})]$, where $A_{non-zero}$ is the amplitude, $\tau_{non-zero}$ is the lifetime of the aggregate non-zero FRET state, and $y_{0,non-zero}$ is the offset. The apparent rate of IF2 dissociation, $k_{d,app}$ is given by $1/\tau_{non-zero}$. The apparent equilibrium dissociation constant for IF2 binding, $K_{d,app}$, is calculated by dividing $k_{d,app}$ by $k_{a,app}$.

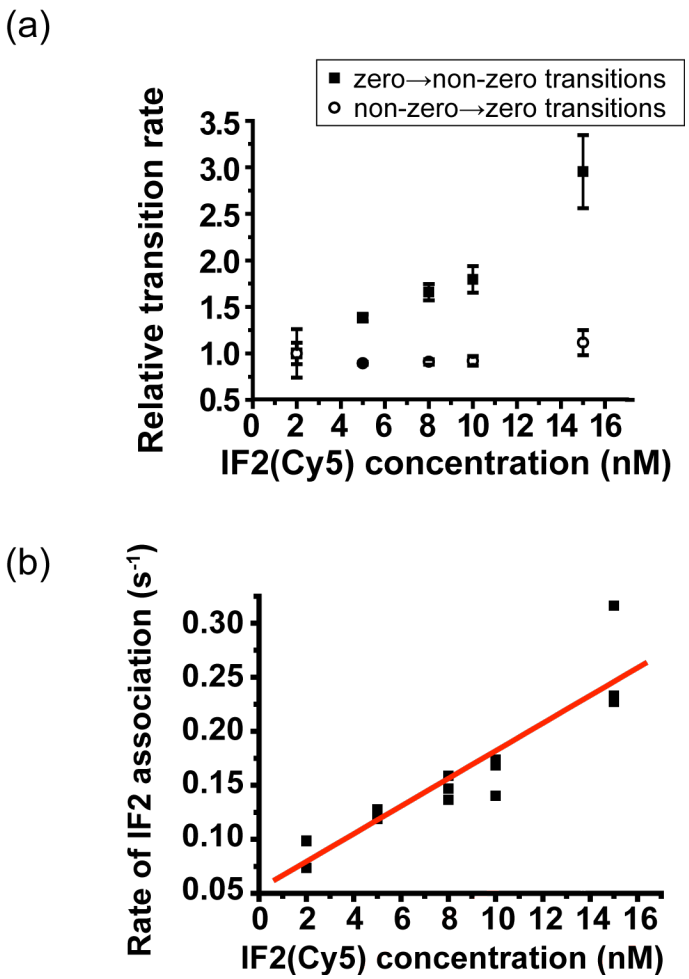

Supplementary Figure 6. (a) Dependence of the 30S $IC_{-1/3}$ zero→non-zero and non-zero→zero FRET transition rates on the concentration of IF2(Cy5). 30S $IC_{-1/3}$ was assembled and smFRET experiments were carried out as described in the Materials and Methods, with the exception that the concentration of IF2(Cy5) added to each flowcell varied from 2 nM to 15 nM as indicated along the *x* axis. The resulting E_{FRET} trajectories were analyzed as described in Supplementary Note 3 to obtain the zero→non-zero and non-zero→zero FRET transition rates. For clearer visualization, the zero→non-zero and non-zero→zero FRET transition rates were normalized to the zero→non-zero and non-zero→zero FRET transition rates obtained at 2 nM IF2(Cy5), respectively. The relative zero→non-zero FRET transition rates were plotted using filled squares and the relative non-zero→zero FRET transition rates were plotted using open circles. The error bars represent the standard deviation of three measurements. Consistent with a bimolecular binding process, the zero→non-zero FRET transition rate increased as a function of increasing IF2(Cy5) concentration. Likewise, consistent with a unimolecular dissociation process, the non-zero→zero FRET transition rate remained constant as IF2(Cy5) concentration was increased. These results reveal that the transitions between the zero FRET state and the aggregate non-zero FRET state that are observed in the E_{FRET} trajectories report on the binding kinetics of IF2(Cy5) to 30S $IC_{-1/3}$. **(b)** Plot of the rate of IF2 association to 30S $IC_{-1/3}$ *versus* IF2(Cy5) concentration. The data were fit with a linear equation (red line) of the form $y = mx + b$ where $m = 0.013 \pm 0.001$ $nM^{-1}s^{-1}$ is the slope and $b = 0.05 \pm 0.01$ s^{-1} is the y offset. The numerical value of *m* provides an estimate of $k_{a,app} = 13 \pm 1$ $\mu M^{-1}s^{-1}$ for the binding of IF2(Cy5) to 30S $IC_{-1/3}$.

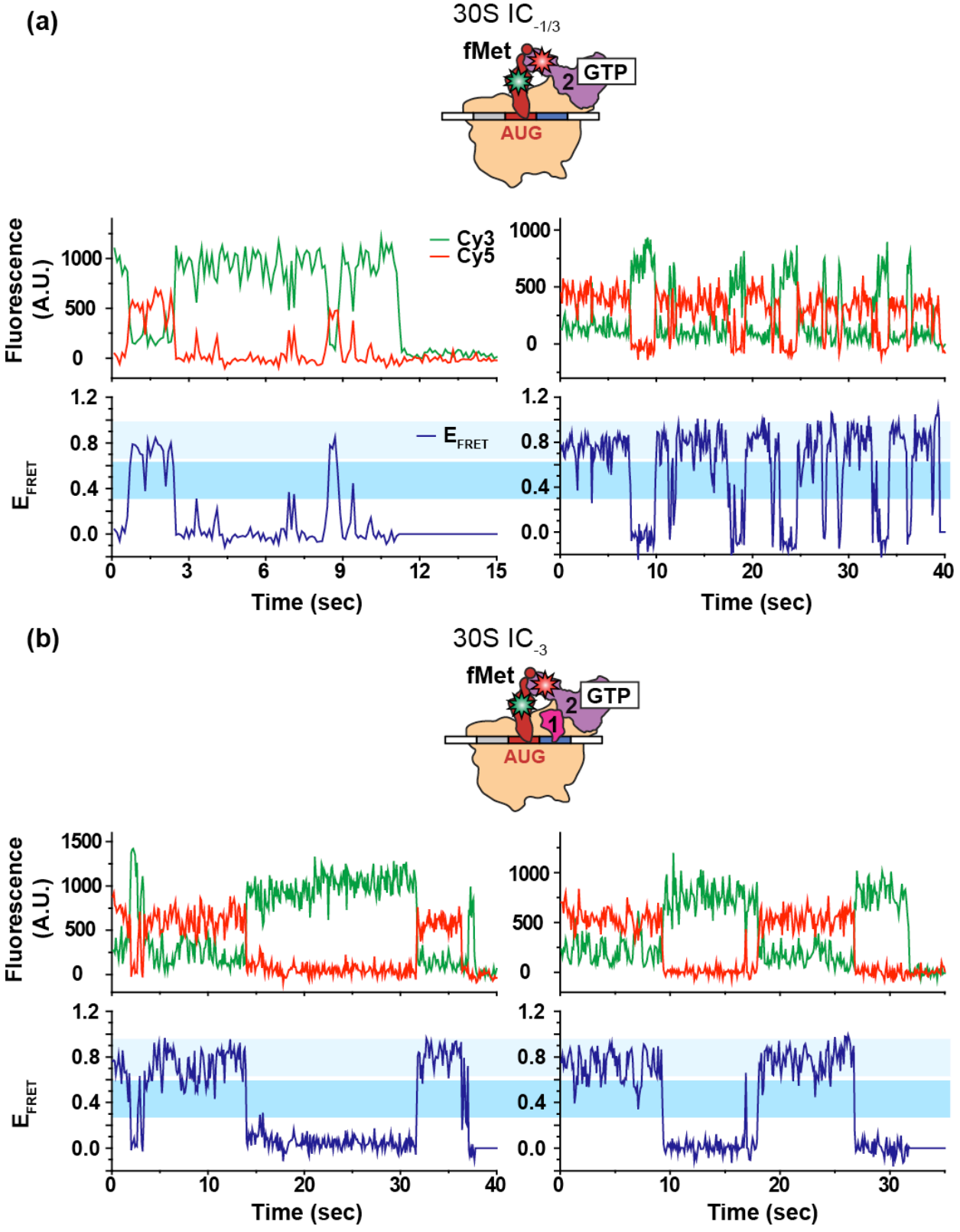
(a)
30S IC-1/3
fMet
GTP
2
AUG
Fluorescence (A.U.)
Cy3
Cy5
E_FRET
Time (sec)
(b)
30S IC-3
fMet
GTP
2
1
AUG
Fluorescence (A.U.)
E_FRET
Time (sec)

Supplementary Figure 7. Typical Cy3 and Cy5 emission intensities *versus* time and E_{FRET} *versus* time trajectories that exhibit fluctuations between IF2-$tRNA_{0.5,c}$ and IF2-$tRNA_{0.8,c}$ configurations of the IF2•tRNA sub-complex. Cartoons depict the IF2-bound form of each of the 30S ICs investigated (first row). Representative Cy3 (green) and Cy5 (red) emission intensities *versus* time trajectories (second row) and the corresponding E_{FRET} *versus* time trajectories (third row) are plotted as described in Supplementary Figure 5a. The E_{FRET} region corresponding to the IF2-$tRNA_{0.8,c}$ configuration of the IF2•tRNA sub-complex is shaded in light cyan and the E_{FRET} region corresponding to the IF2-$tRNA_{0.5,c}$ configuration of the IF2•tRNA sub-complex is shaded in dark cyan. **(a)** 30S $IC_{-1/3}$. **(b)** 30S IC_{-3}.

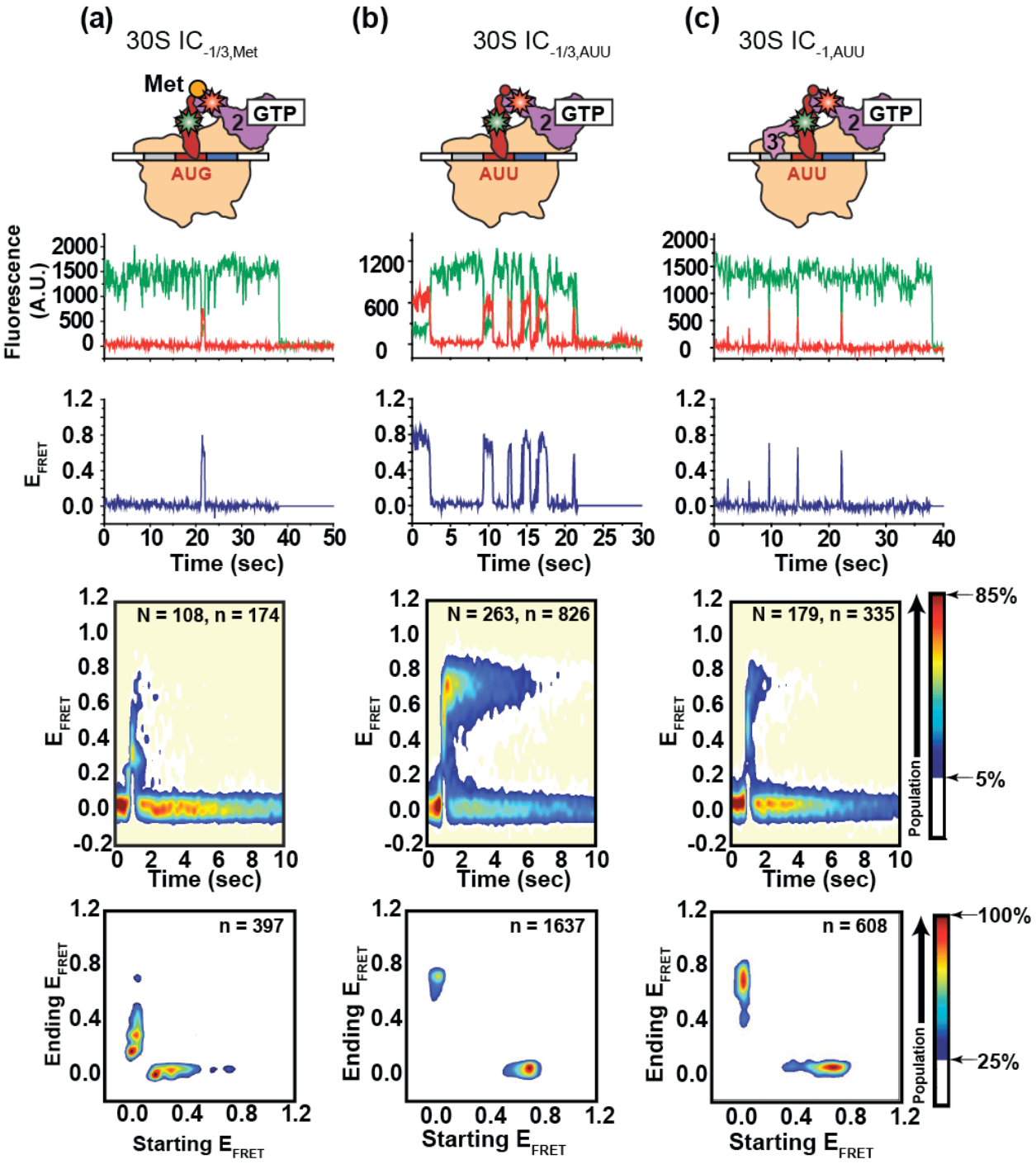

Supplementary Figure 8. The effect of the nature of the P site tRNA and the identity of the P site codon on the stability of IF2 and the conformational dynamics of the IF2•tRNA sub-complex. Cartoons depict the IF2-bound form of each of the 30S ICs investigated (first row). Representative Cy3 (green) and Cy5 (red) emission intensities *versus* time trajectories (second row), the corresponding E_{FRET} *versus* time trajectories (third row), the surface contour plots of the time evolution of population FRET arising from post-synchronization of IF2 binding events

(fourth row), and the transition density plots (fifth row) are plotted as described in Supplementary Figure 5a. **(a)** 30S $IC_{-1/3,Met}$, **(b)** 30S $IC_{-1/3,AUU}$, and **(c)** 30S $IC_{-1,AUU}$.

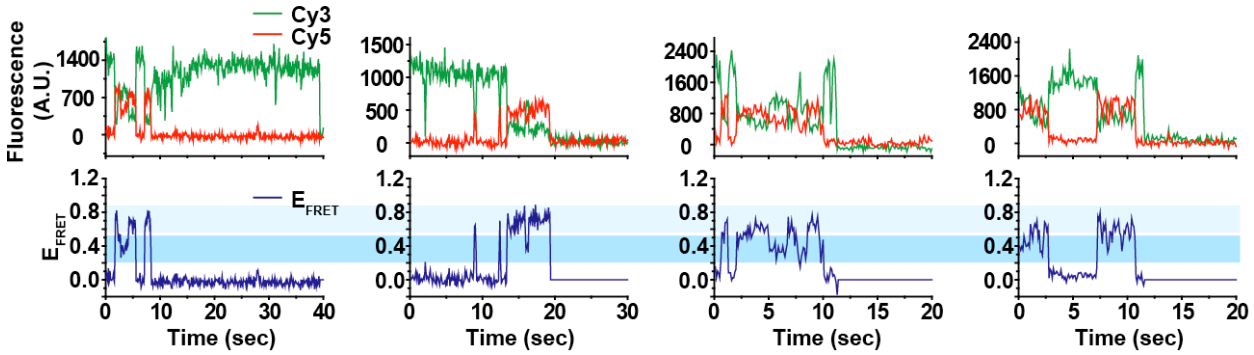

Supplementary Figure 9. Typical Cy3 and Cy5 emission intensities *versus* time and E_{FRET} *versus* time trajectories of 30S $IC_{C,AUU}$ that exhibit transitions between two non-zero FRET states centered at an E_{FRET} value of 0.4 ± 0.3 and 0.7 ± 0.1. Representative Cy3 (green) and Cy5 (red) emission intensities *versus* time trajectories (first row) and the corresponding E_{FRET} *versus* time trajectories (second row) are plotted as described in Supplementary Figure 5a. The E_{FRET} region corresponding to the E_{FRET} = 0.7 ± 0.1 is shaded in light cyan and the FRET region corresponding to the E_{FRET} = 0.4 ± 0.3 is shaded in dark cyan.

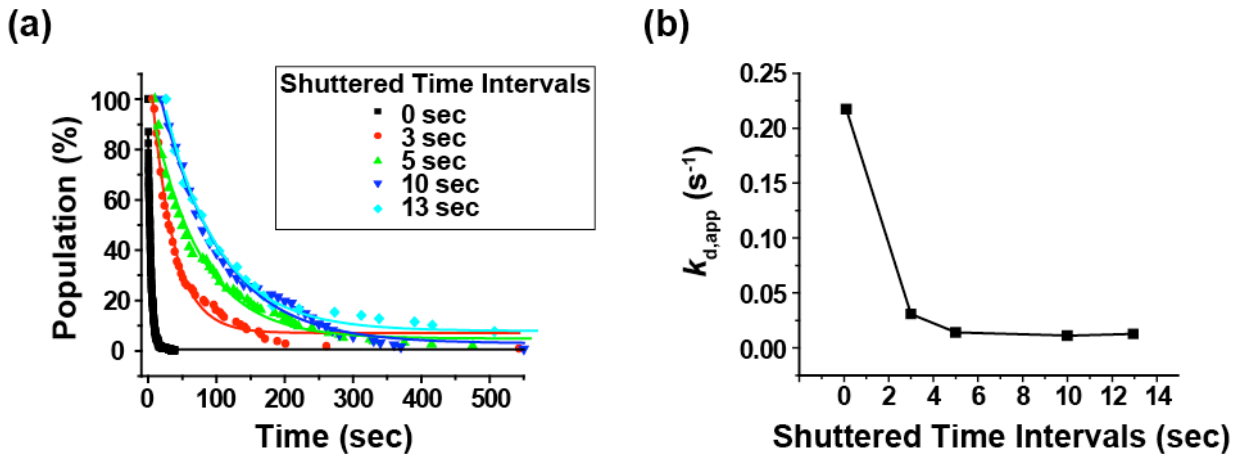

Supplementary Figure 10. Measurement of $k_{d,app}$ for 30S IC_C using shuttered laser excitation. **(a)** Curve-fitting population decay histograms of the number of 30S ICs in the aggregate non-zero FRET state prior to photobleaching or transitioning to the zero FRET state as a function of time for five different shuttered time intervals. These pre-steady-state smFRET experiments were performed as described in Supplementary Note 3. The histograms were generated from the number of 30S ICs in the aggregate non-zero FRET state that were observed prior to photobleaching or transitioning to the zero FRET state as a function of time using shuttered time intervals of 0 sec (*i.e.*, continuous laser excitation), 3 sec, 5 sec, 10 sec, and 13 sec as indicated in the legend. The resulting five histograms were all well described by single-exponential decays (solid colored curves) of the form $y = y_{0,non-zero} + A_{non-zero}[\exp(-x/\tau_{non-zero})]$, where $y_{0,non-zero}$ is the offset, $A_{non-zero}$ is the amplitude, and $\tau_{non-zero}$ is the lifetime of the aggregate non-zero FRET state prior to photobleaching or transitioning to the zero FRET state. The corresponding $k_{d,app}$ is given by $1/\tau_{non-zero}$. **(b)** Plot of $k_{d,app}$ *versus* the shuttered time interval. Experimental values of $k_{d,app}$ at different shuttered time intervals are connected by straight lines as a guide to the trend of change. Consistent with the interpretation that the measurement of $k_{d,app}$ using continuous laser excitation is limited by photobleaching, $k_{d,app}$ is observed to decrease as the shuttered time interval is increased. $k_{d,app}$ continues to decrease as a function of increasing shuttered time interval until a shuttered time interval of ~5 sec, beyond which the value of $k_{d,app}$ is observed to plateau, indicating that the measurement is no longer limited by photobleaching and reflects the true $k_{d,app}$ (0.013 s^{-1}).

SUPPLEMENTARY TABLES

Supplementary Table 1. Comparison of the association rate constants ($k_{a,app}$s), dissociation rate constants ($k_{d,app}$s), and dissociation equilibrium constants ($K_{d,app}$s) for the interaction of IF2 with 30S ICs carrying different combinations of IFs, tRNAs, and start codons obtained using the curve fitting-based and the transition probability matrix-based population decay analyses described in Supplementary Note 3.

Complex	$k_{a,app}$ ($\mu M^{-1}s^{-1}$)		$k_{d,app}$ (s^{-1})		$K_{d,app}$ (nM)	
	Curve fitting	Transition probability matrix	Curve fitting	Transition probability matrix	Curve fitting	Transition probability matrix
30S $IC_{-1/3}$	13±1	11.3±0.5	0.8±0.2	1.16±0.05	70±10	103±6
30S IC_{-3}	5.3±0.6	3.7±0.2	0.20±0.01	0.27±0.01	39±5	73±6
30S IC_{-1}	3.32±0.03	3.1±0.1	2.1±0.3	1.8±0.1	600±100	600±50
30S IC_{C}	3.9±0.1	3.3±0.3	0.220±0.003	0.32±0.02	57±2	97±9
30S $IC_{-1/3,Met}$	1.6±0.02	1.5±0.1	1.4±0.3	1.3±0.3	800±200	800±200
30S $IC_{-3,Met}$	3.13±0.05	2.1±0.1	1.5±0.2	1.5±0.1	470±50	710±80
30S $IC_{-3,Phe}$	2.28±0.02	1.38±0.09	1.6±0.2	1.30±0.15	690±70	900±100
30S $IC_{-1/3,AUU}$	8.7±0.8	6.8±0.5	0.59±0.04	0.67±0.04	68±8	98±9
30S $IC_{-3,AUU}$	5.5±0.2	4.1±0.4	0.35±0.02	0.44±0.03	63±4	110±10
30S $IC_{-1,AUU}$	4.27±0.04	4.3±0.3	2.0±0.3	1.6±0.2	470±70	370±40
30S $IC_{C,AUU}$	4.2±0.1	4.5±0.2	0.65±0.06	0.65±0.04	160±20	140±10

Supplementary Table 2. Rate constants describing transitions from the IF2-tRNA$_{0.5,c}$ to the IF2-tRNA$_{0.8,c}$ configurations of the IF2•tRNA sub-complex ($k_{0.5,c\rightarrow0.8,c}$), rate constants describing transitions from the IF2-tRNA$_{0.8,c}$ to the IF2-tRNA$_{0.5,c}$ configurations of the IF2•tRNA sub-complex ($k_{0.8,c\rightarrow0.5,c}$), and equilibrium constants describing the equilibrium between the IF2-tRNA$_{0.5,c}$ and IF2-tRNA$_{0.8,c}$ configurations of the IF2•tRNA sub-complex (K_{eq} = $k_{0.8,c\rightarrow0.5,c}$ / $k_{0.5,c\rightarrow0.8,c}$) within 30S IC$_{-1/3}$, 30S IC$_{-3}$, and 30S IC$_C$.

Complex	$k_{0.5,c\rightarrow0.8,c}$ (s^{-1})	$k_{0.8,c\rightarrow0.5,c}$ (s^{-1})	K_{eq}
30S IC$_{-1/3}$	4.4±0.4	0.49±0.06	0.11±0.02
30S IC$_{-3}$	3.0±0.5	0.39±0.04	0.13±0.03
30S IC$_C$	1.3±0.1	0.96±0.07	0.74±0.08

Supplementary Table 3. Final concentrations to which 30S ICs were diluted, expressed in terms of aa-tRNA(Cy3) concentrations, for loading into flowcells for surface tethering. The final concentration of each 30S IC was optimized such that the surface-tethering procedure described in the Materials and Methods generated ~300 surface-tethered 30S ICs per field-of-view (FOV = 60 × 120 μm). Due to the decreased stability of aa-tRNA within 30S ICs assembled in the presence of IF3[4] and/or near-cognate start codons[5] 30S ICs assembled in the presence of IF3 and/or formed using $mRNA_{AUU}$ required significantly higher concentrations for surface tethering than the 0.2-0.3 nM which were required for surface tethering of 30S ICs assembled in the absence of IF3 and/or using $mRNA_{AUG}$.

Complex	aa-tRNA(Cy3) Concentration (nM)
30S IC_{-3}	~0.2
30S $IC_{-1/3}$	~0.3
30S $IC_{-3,Phe}$	~0.3
30S $IC_{-3,Met}$	~0.3
30S $IC_{-1/3,Met}$	~0.3
30S IC_{-1}	~0.6
30S $IC_{-1/3,AUU}$	~1.0
30S $IC_{-3,AUU}$	~1.6
30S IC_{C}	~2.0
30S $IC_{-1,AUU}$	~2.4
30S $IC_{C,AUU}$	~2.4

SUPPLEMENTARY NOTES

Supplementary Note 1. mRNAs used in the present study.

The mRNAs used for the biochemical and single-molecule fluorescence microscopy experiments presented in this work were all variants of the naturally occurring mRNA that encodes gene product 32 from T4 bacteriophage (T4 gp32) and that has been previously described and used in our laboratory's single-molecule fluorescence microscopy studies of translation initiation[3,10,11]. The three mRNAs used for single-molecule fluorescence microscopy experiments were chemically synthesized (Dharmacon, Inc.). Two of these mRNAs ($mRNA_{AUG}$ and $mRNA_{AUU}$) contained a 5'-biotin modification that enabled tethering of the corresponding 30S ICs to the streptavidin-derivatized surface of the flowcells used for imaging by TIRF microscopy and differed only in the identity of the start codon (AUG in the case of $mRNA_{AUG}$ and AUU in the case of $mRNA_{AUU}$). The third of these mRNAs ($mRNA_{AUG(–bio)}$) contains an AUG start codon but lacks a 5'-biotin, thus serving as a control mRNA with which to test the biotin specificity of 30S IC tethering to the streptavidin-derivatized surface of the flowcells. The complete sequences of all three mRNAs are provided below. In addition, the mRNAs used by Ehrenberg and co-workers[4,12], Rodnina and co-workers[13], and Cooperman and co-workers[14] in the ensemble kinetic studies referenced throughout the manuscript are shown below for comparative purposes. In each mRNA the Shine-Dalgarno ribosomal binding site is underlined in italics and the start codon is underlined in bold.

The current study:

$mRNA_{AUG}$:

5'Biotin-CAACCUAAAACUUACACAAAUUAAA*AAGGAAAU*AGAC**AUG**UUCAAAGUCGAAAAA UCUACUGCU-3'

$mRNA_{AUU}$:

5'Biotin-CAACCUAAAACUUACACAAAUUAAAAAGGAAAUAGAC**AUU**UUCAAAGUCGAAAAA UCUACUGCU-3'

$mRNA_{AUG(–bio)}$:

5'-GCAACCUAAAACUUACACAGGGCCCU*AAGGAAAU*AAAA**AUG**UUUAA A-3'

Ehrenberg and co-workers[4,12]:

MFTI mRNA:

5'-GGGAAUUCGGGCCCUUGUUAACAAU*UAAGGAGGU*AUACU**AUG**UUUACGAUUUAAUUG CAGAAAAAAAAAAAAAAAAAAAA-3'

Rodnina and co-workers[13] and Cooperman and co-workers[14]:

m002 AUG

5'-... CAA UUA *AGG AGG UA*U ACU **AUG** UUU ACG AUU ...-3'

m002 AUU

5'-... CAA UUA *AGG AGG UA*U ACU **AUU**UUU ACG AUU ...-3'

m022 AUG ...

5'-UUA AC*A GGU A*UA CAU ACU **AUG** UUU ACG AUU ...-3'

m022 AUU

5'-... UUA AC*A GGU A*UA CAU ACU **AUU** UUU ACG AUU ...-3'

The mRNA used for the primer extension inhibition, or "toeprinting",-based IF2 activity assay ($mRNA_{pri-ext}$, see Supplementary Fig. 2) was *in vitro* transcribed using T7 RNA polymerase and a linearized plasmid DNA template generated by BamH1 digestion of a plasmid encoding a variant of T4 gp32 under the control of a T7 polymerase promoter using previously described protocols[3,15-17]. The sequence of $mRNA_{pri-ext}$ is provided below (The Shine-Dalgarno ribosomal binding site is underlined in italics, the start codon is underlined in bold, and the primer binding site for the primer extension inhibition assay is underlined in bold italics):

$mRNA_{pri-ext}$

5'GGCAACCUAAAACUUACACAGGGCCCU*AAGGAAAU*AAAA**AUG**UUUAAAGAAGUAUACAC
UGCUGAACUCGCUGCACAAAUGG***CUAAACUGAAUGGCAAUA***AAGGUUUUUCUUCUGAA
GAUAAAGGCGAGUGGAAACUGAAACUCGAUAAUGCGGGUAACGGUCAAGCAGUAAUUCG
UUUUCUUCCGUCUAAAAAUGAUGAACAAGCACCAUUCGCAAUUCUUGUAAAUCACGGUU
UCAAGAAAAAUGGUAAAUGGUAUAUUGAAACAUGUUCAUCUACCCAUGGUGAUUACGAU
UCUUGCCCAGUAUGUCAAUACAUCAGUAAAAAUGAUCUAUACAACACUGACAAUAAAGAG
UACAGUCUUGUUAAACGUAAAACUUCUUACUGGGCUAACAUUCUUGUAGUAAAAGACCC
AGCUGCUCCAGAAAACGAAGGUAAAGUAUUUAAAUACCGUUUCGGUAAGAAAAUCUGGG
AUAAAAUCAAUGCAAUGAUUGCGGUUGAUGUUGAAAUGGGUGAAACUCCAGUUGAUGUA
ACUUGUCCGUGGGAAGGUGCUAACUUUGUACUGAAAGUUAAACAAGUUUCUGGAUUUA
GUAACUACGAUGAAUCUAAAUUCCUGAAUCAAUCUGCGAUUCCAAACAUUGACGAUGAA
UCUUUCCAGAAAGAACUGUUCGAACAAAUGGUCGACCUUUCUGAAAUGACUUCUAAAGA
UAAAUAAGG3'

Supplementary Note 2. Determination of the number of FRET states present in the set of E_{FRET} trajectories corresponding to each 30S IC and the centers of each of these FRET states.

A preliminary estimate of the number of FRET states present in the set of E_{FRET} trajectories corresponding to each 30S IC was obtained by plotting a one-dimensional E_{FRET} histogram in which the range of –0.2 to 1.2 E_{FRET} was separated into 70 bins (Supplementary Fig. 5b). With the exception of 30S $IC_{-1/3}$ and 30S $IC_{C,AUU}$, the E_{FRET} histograms were built by counting the frequency with which the time points encompassing each of the E_{FRET} trajectories within an entire dataset of E_{FRET} trajectories occupy the range of E_{FRET} values specified by each bin. For 30S $IC_{-1/3}$ and 30S $IC_{C,AUU}$, the E_{FRET} histograms were built using only the subset of E_{FRET} trajectories that exhibited transitions between non-zero FRET states (Supplementary Fig. 7 and 9). E_{FRET} histograms were normalized to the most populated bin. The resulting E_{FRET} histograms were fitted with multiple Gaussian distributions using Origin 7.0 in order to obtain the center and full-width-at-half-maximum of each Gaussian peak. The maximum number of FRET states identified in any of the 30S ICs using this approach was three, (one zero FRET state and two non-zero FRET states), identified in the set of E_{FRET} trajectories corresponding to 30S IC_C, 30S $IC_{C,AUU}$, 30S IC_{-3}, 30S $IC_{-3,AUU}$, 30S $IC_{-1/3}$, and 30S $IC_{-1/3,AUU}$.

To more rigorously determine the number of FRET states present in individual E_{FRET} trajectories, each raw E_{FRET} trajectory was idealized using the hidden Markov model (HMM) algorithm implemented within the software program HaMMy[6] (Supplementary Fig. 5c) with an initial estimate of five FRET states (*i.e.*, two additional FRET states over the maximum number of FRET states determined by visual inspection of the one-dimensional E_{FRET} histograms

constructed from the raw E_{FRET} trajectories) and a maximum likelihood-based algorithm for selecting the most probable number of FRET states present in the raw E_{FRET} trajectory. Using this approach, the majority (~55%) of the raw E_{FRET} trajectories observed for 30S IC_C, the 30S IC which exhibited the largest number of FRET states through visual inspection, were best modeled by HMMs with three or fewer states corresponding to E_{FRET} = 0 ± 0.04, 0.5 ± 0.2, and 0.8 ± 0.1. Visual inspection of the remaining ~45% of raw E_{FRET} trajectories which were best modeled by HMMs with four or five states strongly suggested that these E_{FRET} trajectories were in fact well described using only the three previously identified FRET states centered at E_{FRET} = 0 ± 0.04, 0.5 ± 0.2, or 0.8 ± 0.1 and had simply been overfitted to an additional one or two states by the maximum likelihood-based, HMM algorithm implemented in HaMMy. Consistent with this conclusion, idealization of each raw E_{FRET} trajectory from the 30S ICs exhibiting the largest number of FRET states (*i.e.*, 30S IC_{-3} and 30S IC_C) using the HMM algorithm software program vbFRET[7], which significantly minimizes overfitting by using a maximum evidence-based algorithm for selecting the most probable number of FRET states present in the raw E_{FRET} trajectory[7,8], significantly minimized the fraction of raw E_{FRET} trajectories that were best modeled by HMMs with four or five states from ~45% to ~10%.

Supplementary Note 3. Calculation of apparent IF2 association rate constants ($k_{a,app}$) and dissociation rate constants ($k_{d,app}$)

$k_{a,app}$ and $k_{d,app}$ for the interaction of IF2 with each 30S IC (Table 1 and Supplementary Table 1) were determined from steady-state smFRET data using curve fitting-based population decay analyses analogous to those which we have previously described[18,19] and that are based upon a stochastic description of the reaction kinetics[20-23]. Briefly, idealized E_{FRET} trajectories were first post-processed exactly as described for the TDP plots in Supplementary Fig. 5e. A threshold of E_{FRET} = 0.2 was then applied to each idealized and post-processed E_{FRET} trajectory such that each trajectory was divided into time periods spent in the zero FRET state (E_{FRET} < 0.2), corresponding to the IF2-free state of the 30S IC, prior to transitioning into any non-zero FRET state (E_{FRET} ≥ 0.2), corresponding to the IF2-bound state of the 30S IC, and time periods spent in the aggregate non-zero FRET state prior to transitioning into the zero FRET state. The threshold of E_{FRET} = 0.2 was chosen based on visual inspection of the entire set of one-dimensional E_{FRET} histograms corresponding to all of the 30S ICs analyzed in this work, which revealed that E_{FRET} = 0.2 corresponded to the value of the E_{FRET} that most optimally separated the Gaussian distribution corresponding to the zero FRET state completely from the Gaussian distributions corresponding to the non-zero FRET states in the one-dimensional E_{FRET} histograms. Note that, for the purposes of this analysis, the two non-zero FRET states which we have observed centered at E_{FRET} = 0.5 and E_{FRET} = 0.8 were clustered into the single, aggregate non-zero FRET state defined by E_{FRET} ≥ 0.2 and corresponding to the IF2-bound state of the 30S IC. A population decay histogram of the number of 30S ICs in the zero FRET state prior to transitioning to any non-zero FRET state as a function of time was generated using the entire set of idealized E_{FRET} trajectories associated with each 30S IC sample (Supplementary Fig. 5f). For each 30S IC sample, the histogram was well described by a single-exponential function of the form $y = y_{0,zero} + A_{zero}[\exp(-x/\tau_{zero})]$, where A_{zero} is the amplitude, τ_{zero} is the lifetime, and $y_{0,zero}$ is the offset (Supplementary Fig. 5f). $k_{a,app}$ was obtained by calculating the inverse of the product of τ_{zero} and the concentration of IF2(Cy5) present in the flowcell. Likewise, the population decay histogram of the number of 30S ICs in the aggregate non-zero FRET state prior to transitioning to the zero FRET state as a function of time for each 30S IC sample was well described by a single-exponential function of the form $y = y_{0,non-zero} + A_{non-zero}[\exp(-x/\tau_{non-zero})]$ (Supplementary Fig. 5f), with the inverse of $\tau_{non-zero}$ providing $k_{d,app}$ directly. This single exponential-function fitting process is the same as equating the measured population decay of the zero FRET state or the aggregated non-zero FRET state to the survival function for a

Markov process[24]. We note that, for each E_{FRET} trajectory, the data between the start of the observation period and the first transition as well as the data between the last transition and Cy3 photobleaching or the end of the observation period were not included in the histograms due to the arbitrary onset of the observation period, the stochastic nature of photobleaching events, and the arbitrary conclusion of the observation period. In addition, it is important to note that Cy5 photobleaching is also stochastic, which results in a systematic underestimation of the number of 30S ICs in the aggregate non-zero FRET state prior to transitioning to the zero FRET state as a function of time and thus an overestimation of k_d. Likewise, stochastic Cy5 photobleaching results in a systematic overestimation of the number of 30S ICs in the zero FRET state prior to transitioning to any non-zero FRET state as a function of time and thus an underestimation of k_a. Primarily as a result of this limitation, all k_a, k_d, and, consequently, K_d values are conservative estimates and are thus reported as "apparent" values ($k_{a,app}$, $k_{d,app}$, and $K_{d,app}$, respectively).

The curve fitting-based population decay analysis of steady-state smFRET data recorded using continuous laser excitation described above has several important limitations which did not allow us to apply it uniformly for determination of $k_{a,app}$ and $k_{d,app}$ in all of the 30S IC samples which we have investigated. For example, the binding of IF2 to 30S IC_C is exceptionally stable and long-lived, such that the rate of Cy5 photobleaching (~0.2 s^{-1}) is much faster than the rate of IF2 dissociation, thus limiting our ability to accurately determine $k_{d,app}$. To circumvent this limitation, we collected a series of pre-steady-state smFRET experiments using 30S IC_C. In these experiments, Tris-Polymix Buffer supplemented with IF1 and IF3, as well as with the oxygen-scavenging system and triplet-state quencher cocktail described in the Materials and Methods, was stopped-flow delivered into the flowcell in order to remove any IF2(Cy5) that was not bound to the surface-tethered 30S IC_C. Prior to the stopped-flow delivery, three consecutive images of the surface-tethered 30S IC_C were acquired using continuous laser excitation and a time resolution of 100 ms $frame^{-1}$. This was followed by stopped-flow delivery and TIRF imaging under conditions in which the laser excitation source was shuttered so as to provide an exposed time interval of 100 ms $frame^{-1}$ for each image and a shuttered time interval that was varied from 0–13 sec between each frame for a total observation period of 15–20 min. The E_{FRET} trajectories in each shuttered experiment were thresholded at E_{FRET} = 0.2 and, in each case, a histogram of the number of 30S ICs in the aggregate non-zero FRET state prior to photobleaching or transitioning to the zero FRET state as a function of time was well described by a single-exponential function of the form $y = y_{0,non-zero} + A_{non-zero}[\exp(-x/\tau_{non-zero})]$ (Supplementary Fig. 6a), with the inverse of $\tau_{non-zero}$ providing $k_{d,app}$ directly. A plot of $k_{d,app}$ *versus* the shuttered time interval reveals that $k_{d,app}$ decreases as the shuttered time interval is increased, as would be expected if the measurement of $k_{d,app}$ is limited by photobleaching, until a shuttered time interval of ~5 sec. Beyond a shuttered time interval of 5 sec, the value of $k_{d,app}$ is observed to plateau, indicating that the measurement is no longer limited by photobleaching and now reflects the true $k_{d,app}$ (0.013 s^{-1}) (Supplementary Fig. 6b).

The stable and long-lived binding of IF2 to 30S IC_C that was described in the previous paragraph also results in very rare excursions of the E_{FRET} trajectories to the zero FRET state corresponding to the IF2-free state of 30S IC_C during steady-state smFRET experiments. Consequently, it is difficult to accurately measure the number of 30S ICs in the zero FRET state prior to transitioning to the aggregate non-zero FRET state as a function of time using steady-state smFRET experiments, thus limiting the accurate determination of $k_{a,app}$ using the curve fitting-based population decay analysis described above for steady-state smFRET data. To circumvent this limitation, we performed a pre-steady-state smFRET experiment in which a 30S IC containing 30S subunits, fMet-tRNA(Cy3)^{fMet}, IF1, IF3, and $mRNA_{AUG}$ (*i.e.*, a 30S IC analogous to 30S IC_C, but lacking IF2) was prepared, diluted, loaded into flowcells, incubated, and washed as described in the Materials and Methods, with the exception that 50 nM IF2(Cy5)

was not included in the final wash step. Instead, after imaging this 30S IC for 3 frames, 100 μL of 50 nM IF2(Cy5) in Tris-Polymix Buffer supplemented with IF1 and IF3, as well as with the oxygen-scavenging system and triplet state quencher cocktail described in the Materials and Methods, was stopped-flow delivered into the flowcells containing the surface-tethered 30S ICs and the real-time arrival of IF2(Cy5) to individual 30S ICs, reported by the first time point at which $E_{FRET} \geq 0.2$, was monitored. A population decay histogram of the number of 30S ICs exhibiting an $E_{FRET} < 0.2$ prior to transitioning to $E_{FRET} \geq 0.2$ as a function of time was well-described by a single-exponential fit of the form $y = y_{0,zero} + A_{zero}[\exp(-x/\tau_{zero})]$, with the inverse of the product of τ_{zero} and the concentration of IF2 providing $k_{a,app}$ for 30S IC_C.

Similar limitations to those described in the previous two paragraphs are encountered in 30S IC samples that spend most of their time in the zero FRET state corresponding to the IF2-free state of the 30S IC, only rarely undergoing transitions to a non-zero FRET state corresponding to the IF2-bound state of the 30S IC (*i.e.*, 30S $IC_{-3,Met}$, 30S $IC_{-3,Phe}$, and 30S $IC_{-1/3,Met}$). In this case, the rate of Cy3 photobleaching (~0.15 s^{-1}) is presumably much faster than the rate of IF2 association, thus producing a significant sub-population of E_{FRET} trajectories originating from 30S ICs that are capable of binding IF2, but that fail to do so during the observation time. For this sub-population of E_{FRET} trajectories, the entire observation period represents a fraction of a very long time that the corresponding 30S ICs spend in the zero FRET state prior to transitioning to the aggregate non-zero FRET state. Failure to include these 30S ICs and the very long times that they spend in the zero FRET state prior to transitioning to the aggregate non-zero FRET state, as is the case when using the curve fitting-based population decay analysis described above, results in a significant over-estimation of $k_{a,app}$. To circumvent this limitation, we have used a transition probability matrix-based population decay analysis to calculate corrected values of $k_{a,app}$ for 30S $IC_{-3,Met}$, 30S $IC_{-3,Phe}$, and 30S $IC_{-1/3,Met}$.

We began by thresholding the idealized, but not post-processed, E_{FRET} trajectories into time periods spent in the zero FRET state ($E_{FRET} < 0.2$), corresponding to the IF2-free state of the 30S IC, prior to transitioning into any non-zero FRET state ($E_{FRET} \geq 0.2$), corresponding to the IF2-bound state of the 30S IC, and time periods spent in the aggregate non-zero FRET state prior to transitioning into the zero FRET state, as described above. The thresholded, idealized E_{FRET} trajectories were next used to construct a 2 × 2 counting matrix:

$$\text{Counting Matrix} = \begin{bmatrix} n_{\text{zero}\rightarrow\text{zero}} & n_{\text{zero}\rightarrow\text{non-zero}} \\ n_{\text{non-zero}\rightarrow\text{zero}} & n_{\text{non-zero}\rightarrow\text{non-zero}} \end{bmatrix}$$

The matrix elements, n_{ij}, report the total number of times the E_{FRET} signal is observed to be in state *i* at time *t* and state *j* at time *t*+1 in the entire set of idealized E_{FRET} trajectories associated with each 30S IC sample. Row normalization of the counting matrix such that the matrix elements across each row sum to 1 provides the transition probability matrix and ensures that the probability of remaining in state *i* and the probability of transitioning out of state *i* sum to 1.

$$\text{Transition Probability Matrix} = \begin{bmatrix} p_{\text{zero}\rightarrow\text{zero}} & p_{\text{zero}\rightarrow\text{non-zero}} \\ p_{\text{non-zero}\rightarrow\text{zero}} & p_{\text{non-zero}\rightarrow\text{non-zero}} \end{bmatrix}$$

The transition probability matrix elements, p_{ij} report the probability of transitioning from state *i* at time *t* to state *j* at time $t+\tau$ during a discrete time interval, τ. Thus, the diagonal entries contain the probability of remaining in the i^{th} state at time $t+\tau$. The transition probabilities along the diagonal, $p_{\text{zero}\rightarrow\text{zero}}$ and $p_{\text{non–zero}\rightarrow\text{non–zero}}$, can be converted to $k_{a,app}$ and $k_{d,app}$, respectively, by

relating the diagonal elements of the transition probability matrix (*i.e.*, the probability of remaining in the i^{th} state during a time interval, τ) to the ensemble decay probability for a Markov process during that time interval, using the following equation:

$$p_{\tau} = \exp(-k \bullet \tau)$$

where p_{τ} is the probability that, given the FRET states at time t, no transitions will occur in the time interval between t and $t+\tau$ and k is the reaction rate constant[24]. Thus, in the present case:

$$k_{a,app} = -\ln(p_{zero \rightarrow zero})/[IF2]\tau$$

and

$$k_{d,app} = -\ln(p_{non-zero \rightarrow non-zero})/\tau$$

where τ is set by the data sampling rate (*i.e.*, the time resolution of the smFRET experiments, 100 msec frame^{-1}).

In order to validate the transition probability matrix-based population decay analysis described above, we compared values of $k_{a,app}$ and $k_{d,app}$ obtained using both the curve fitting-based and the transition probability matrix-based population decay analyses of each 30S IC sample. This comparison revealed that the kinetic and thermodynamic parameters ($k_{a,app}$, $k_{d,app}$, and $K_{d,app}$) obtained for each 30S IC using each of the two approaches to the population decay analysis are in very close agreement with each other (Supplementary Table 1).

A straightforward extension of the transition probability matrix-based population decay analysis described above was subsequently used to correct the values of $k_{a,app}$ obtained for 30S $IC_{-3,Met}$, 30S $IC_{-3,Phe}$, and 30S $IC_{-1/3,Met}$. We first determined the fraction of surface-tethered 30S IC_{-3} (as a control for 30S $IC_{-3,Met}$ and 30S $IC_{-3,Phe}$) and the fraction of 30S $IC_{-1/3}$ (as a control for 30S $IC_{-1/3,Met}$) that were capable of transitioning into any non-zero FRET state corresponding to the IF2-bound state of the 30S IC at least once during our observation time (denoted as 30S IC_{-3}^{cap} and 30S $IC_{-1/3}^{cap}$, respectively). The difference between 30S IC_{-3}^{cap} and the fraction of surface-tethered 30S $IC_{-3,Met}$ and 30S $IC_{-3,Phe}$ that are actually observed to transition into any non-zero FRET state corresponding to the IF2-bound state of the 30S IC at least once during our observation time (denoted as 30S $IC_{-3,Met}^{obs}$ and 30S $IC_{-3,Phe}^{obs}$) was assumed to correspond to the fraction of 30S $IC_{-3,Met}$ and 30S $IC_{-3,Phe}$ that were capable of transitioning into any non-zero FRET state corresponding to the IF2-bound state of the 30S IC, but failed to do so during our observation time (denoted as 30S $IC_{-3,Met}^{fail}$ and 30S $IC_{-3,Phe}^{fail}$):

$$30S\ IC_{-3,Met}^{fail} = 30S\ IC_{-3}^{cap} - 30S\ IC_{-3,Met}^{obs} = 0.197 - 0.030 = 0.167$$

$$30S\ IC_{-3,Phe}^{fail} = 30S\ IC_{-3}^{cap} - 30S\ IC_{-3,Phe}^{obs} = 0.197 - 0.027 = 0.170$$

Similarly, the difference between 30S $IC_{-1/3}^{cap}$ and the fraction of surface-tethered 30S $IC_{-1/3,Met}$ that are actually observed to transition into any non-zero FRET state corresponding to the IF2-bound state of the 30S IC at least once during our observation time (denoted as 30S $IC_{-1/3,Met}^{obs}$) was assumed to correspond to the fraction of 30S $IC_{-1/3,Met}$ that were capable of transitioning into any non-zero FRET state corresponding to the IF2-bound state of the 30S IC, but failed to do so during our observation time (denoted as 30S $IC_{-1/3,Met}^{fail}$):

$$30S\ IC_{-1/3,Met}^{fail} = 30S\ IC_{-1/3}^{cap} - 30S\ IC_{-1/3,Met}^{obs} = 0.224 - 0.003 = 0.221$$

We next generated a set of simulated E_{FRET} trajectories corresponding to 30S $IC_{-3,Met}^{fail}$, 30S $IC_{-3,Phe}^{fail}$, and 30S $IC_{-1/3,Met}^{fail}$ in which the number of E_{FRET} trajectories that was simulated for each complex was given by:

$$(N) \times [30S\ IC_{X,Y}^{fail} / 30S\ IC_{X,Y}^{obs}]$$

where N is the total number of E_{FRET} trajectories corresponding to 30S $IC_{X,Y}^{obs}$, the subscript X is -3 or -1/3 (depending on the 30S IC), and the subscript Y is Met or Phe (depending on the 30S IC). To construct a simulated E_{FRET} trajectory, the value of the E_{FRET} signal was set to 0 for every time point and the length of the trajectory was set to the average length of the E_{FRET} trajectories in 30S $IC_{X,Y}^{obs}$ prior to Cy3 photobleaching. Finally, the simulated E_{FRET} trajectories corresponding to 30S $IC_{-3,Met}^{fail}$, 30S $IC_{-3,Phe}^{fail}$, and 30S $IC_{-1/3,Met}^{fail}$ were pooled with the E_{FRET} trajectories corresponding to 30S $IC_{-3,Met}^{obs}$, 30S $IC_{-3,Phe}^{obs}$, and 30S $IC_{-1/3,Met}^{obs}$, respectively, and the transition probability matrix-based population decay analysis described above was used to calculate corrected values of $k_{a,app}$ for 30S $IC_{-3,Met}$, 30S $IC_{-3,Phe}$, and 30S $IC_{-1/3,Met}$ that now include the 30S ICs that are capable of binding IF2, but that fail to do so during the observation time and the very long times that these 30S ICs spend in the zero FRET state prior to transitioning to the aggregate non-zero FRET state. We note that this approach necessarily assumes that: (i) 30S IC_{-3}^{cap} and 30S $IC_{-1/3}^{cap}$ represent the true fractions of 30S IC_{-3} and 30S $IC_{-1/3}$ that are capable of transitioning into any non-zero FRET state corresponding to the IF2-bound state of the 30S IC at least once during our observation time and are not themselves limited by Cy3 photobleaching and (ii) the fraction of 30S $IC_{-3,Met}$ and 30S $IC_{-3,Phe}$ (or 30S $IC_{-1/3,Met}$) that are capable of transitioning into any non-zero FRET state corresponding to the IF2-bound state of the 30S IC at least once during our observation time is the same as 30S IC_{-3} (or 30S $IC_{-1/3}$).

Supplementary Note 4. Determining the uncertainties in measurements of $k_{a,app}$ and $k_{d,app}$

The uncertainties in our measurements of $k_{a,app}$ and $k_{d,app}$ were obtained using a bootstrapping approach. To estimate the uncertainty in $k_{a,app}$ obtained for each 30S IC using the curve fitting-based population decay analysis, a bootstrap sample of the number of 30S ICs in the zero FRET state prior to transitioning to any non-zero FRET state as a function of time was obtained by randomly sampling, with replacement, from the pool of the experimentally observed number of 30S ICs in the zero FRET state prior to transitioning to any non-zero FRET state as a function of time for the corresponding 30S IC. Sampling with replacement was continued until the bootstrap sample contained the same number of 30S ICs in the zero FRET state prior to transitioning to any non-zero FRET state as a function of time as was contained in the original, experimentally derived population decay histogram for the corresponding 30S IC. The number of 30S ICs in the zero FRET state prior to transitioning to any non-zero FRET state as a function of time in the bootstrap sample was then used to construct a new population decay histogram of the number of 30S ICs in the zero FRET state prior to transitioning to any non-zero FRET state as a function of time. This process was repeated 1000 times for each 30S IC, which allowed for the construction of 1000 population decay histograms of the number of 30S ICs in the zero FRET state prior to transitioning to any non-zero FRET state as a function of time for each 30S IC. Each of the 1000 population decay histograms was fitted to obtain 1000 individual estimates of $k_{a,app}$ using the same form of the single-exponential function that was used to obtain $k_{a,app}$ from the original, experimentally derived, population decay histogram of the number of 30S ICs in the zero FRET state prior to transitioning to any non-zero FRET state as a function of time as described in the curve fitting-based population decay analysis outlined in Supplementary Note 3. The standard deviation of these 1000 estimates of $k_{a,app}$ was then reported as the uncertainty in $k_{a,app}$ for each 30S IC. An analogous procedure, except using the set of experimentally determined number of 30S ICs in the aggregate non-zero FRET state prior to transitioning to the zero FRET state as a function of time, was used to determine the uncertainty in $k_{d,app}$ for each 30S IC.

To estimate the uncertainties in $k_{a,app}$ and $k_{d,app}$ obtained for each 30S IC using the transition probability matrix-based population decay analysis, a bootstrap set of E_{FRET} trajectories was obtained by randomly sampling, with replacement, from the experimentally derived set of

idealized, but not post-processed, E_{FRET} trajectories. Sampling with replacement was continued until the bootstrap set of E_{FRET} trajectories contained the same number of E_{FRET} trajectories as was contained in the original, experimentally derived set of idealized, but not post-processed, E_{FRET} trajectories for the corresponding 30S IC. This process was repeated 500 times for each 30S IC, thus allowing the construction of 500 bootstrap sets of E_{FRET} trajectories for each 30S IC. Subjecting each of the 500 bootstrap sets of E_{FRET} trajectories to the transition probability matrix-based population decay analysis described in Supplementary Note 3 then provided 500 individual estimates of $k_{a,app}$ and $k_{d,app}$ for each 30S IC. The standard deviation of these 500 estimates of $k_{a,app}$ and $k_{d,app}$ were then reported as the uncertainties in $k_{a,app}$ and $k_{d,app}$, respectively, for each 30S IC. In the case of 30S $IC_{-1/3,Met}$, 30S $IC_{-3,Met}$, and 30S $IC_{-3,Phe}$, each bootstrap set of E_{FRET} trajectories was generated by sampling, with replacement, only from the set of observed E_{FRET} trajectories corresponding to 30S $IC_{-1/3,Met}^{obs}$, 30S $IC_{-3,Met}^{obs}$, and 30S $IC_{-3,Phe}^{obs}$. The representative E_{FRET} trajectories corresponding to 30S $IC_{-1/3,Met}^{fail}$, 30S $IC_{-3,Met}^{fail}$, and 30S $IC_{-3,Phe}^{fail}$ were subsequently added to each bootstrapped set of E_{FRET} trajectories prior to conducting the transition probability matrix-based population decay analysis.

SUPPLEMENTARY REFERENCES

1. Hartz D., McPheeters D. S., Traut R. & Gold L. (1988). Extension inhibition analysis of translation initiation complexes. *Methods Enzymol* **164**, 419-425.
2. Hartz D., McPheeters D. S. & Gold L. (1989). Selection of the initiator tRNA by Escherichia coli initiation factors. *Genes Dev* **3**, 1899-1912.
3. Fei J., Wang J., Sternberg S. H., MacDougall D. D., Elvekrog M. M., Pulukkunat D. K., Englander M. T. & Gonzalez R. L. (2010). A highly purified, fluorescently labeled in vitro translation system for single-molecule studies of protein synthesis. *Methods Enzymol* **472**, 221-259.
4. Antoun A., Pavlov M. Y., Lovmar M. & Ehrenberg M. (2006). How initiation factors maximize the accuracy of tRNA selection in initiation of bacterial protein synthesis. *Mol Cell* **23**, 183-193.
5. La Teana A., Pon C. L. & Gualerzi C. O. (1993). Translation of mRNAs with degenerate initiation triplet AUU displays high initiation factor 2 dependence and is subject to initiation factor 3 repression. *Proc Natl Acad Sci U S A* **90**, 4161-4165.
6. McKinney S. A., Joo C. & Ha T. (2006). Analysis of single-molecule FRET trajectories using hidden Markov modeling. *Biophys J* **91**, 1941-1951.
7. Bronson J. E., Hofman J. M., Fei J., Gonzalez R. L. & Wiggins C. H. (2010). Graphical models for inferring single molecule dynamics. *BMC Bioinformatics* **11 Suppl 8**, S2.
8. Bronson J. E., Fei J., Hofman J. M., Gonzalez R. L. & Wiggins C. H. (2009). Learning rates and states from biophysical time series: a Bayesian approach to model selection and single-molecule FRET data. *Biophys J* **97**, 3196-3205.
9. Liu Y., Park J., Dahmen K. A., Chemla Y. R. & Ha T. (2010). A comparative study of multivariate and univariate hidden Markov modelings in time-binned single-molecule FRET data analysis. *J Phys Chem B* **114**, 5386-5403.
10. Elvekrog M. M. & Gonzalez R. L. (2013). Conformational selection of translation initiation factor 3 signals proper substrate selection. *Nat Struct Mol Biol* **20**, 628-633.
11. MacDougall D. D. & Gonzalez R. L. (2014). Translation initiation factor 3 regulates switching between different modes of ribosomal subunit joining. *J Mol Biol* .
12. Pavlov M. Y., Zorzet A., Andersson D. I. & Ehrenberg M. (2011). Activation of initiation factor 2 by ligands and mutations for rapid docking of ribosomal subunits. *EMBO J* **30**, 289-301.
13. Milon P., Konevega A. L., Gualerzi C. O. & Rodnina M. V. (2008). Kinetic checkpoint at a late step in translation initiation. *Mol Cell* **30**, 712-720.
14. Grigoriadou C., Marzi S., Pan D., Gualerzi C. O. & Cooperman B. S. (2007). The translational fidelity function of IF3 during transition from the 30 S initiation complex to the 70 S initiation complex. *J Mol Biol* **373**, 551-561.
15. Milligan J. F., Groebe D. R., Witherell G. W. & Uhlenbeck O. C. (1987). Oligoribonucleotide synthesis using T7 RNA polymerase and synthetic DNA templates. *Nucleic Acids Res* **15**, 8783-8798.
16. Wyatt J. R., Chastain M. & Puglisi J. D. (1991). Synthesis and purification of large amounts of RNA oligonucleotides. *Biotechniques* **11**, 764-769.

17. McKenna S. A., Kim I., Puglisi E. V., Lindhout D. A., Aitken C. E., Marshall R. A. & Puglisi J. D. (2007). Purification and characterization of transcribed RNAs using gel filtration chromatography. *Nat Protoc* **2**, 3270-3277.

18. Fei J., Kosuri P., MacDougall D. D. & Gonzalez R. L. (2008). Coupling of ribosomal L1 stalk and tRNA dynamics during translation elongation. *Mol Cell* **30**, 348-359.

19. Fei J., Bronson J. E., Hofman J. M., Srinivas R. L., Wiggins C. H. & Gonzalez R. L. (2009). Allosteric collaboration between elongation factor G and the ribosomal L1 stalk directs tRNA movements during translation. *Proc Natl Acad Sci U S A* **106**, 15702-15707.

20. Delbruck M. (1940). Statistical fluctuation in autocatalytic reactions . **8**, 120-124.

21. McQuarrie D. A. (1967). Stochastic approach to chemical kinetics. *J Appl Prob* **4**, 413-478.

22. Gillespie D. T. (1976). A general method for numerically simulating the time evolution of coupled chemical reactions. *J Comp Phys* **22**, 403-434.

23. Gillespie D. T. (1977). Exact stochastic simulation of coupled chemical reactions. *J Phys Chem* **81**, 2340-2361.

24. van Kampen N. G. (2007). *Stochastic processes in Physics and Chemistry, 3rd Edition*, North Holland Personal Library, JAI press, Greenwich, CT.